PAPER

Resolving a structural issue in cerium-nickel-based oxide: a single compound or a two-phase system?†

Jelena Kojčinović, [ID] [a] Dalibor Tatar, [ID] [a] Stjepan Šarić,[a] Cora Bartus Pravda,[b] Andraž Mavrič, [ID] [c] Iztok Arčon,[c,d] Zvonko Jagličić,[e,f] Maximilian Mellin, [ID] [g] Marcus Einert, [ID] [g] Angela Altomare,[h] Rocco Caliandro, [ID] [h] Ákos Kukovecz, [ID] [b] Jan Philipp Hofmann [ID] [g] and Igor Djerdj [ID] *[a]

CeNiO$_3$ has been reported in the literature in the last few years as a novel LnNiO$_3$ compound with promising applications in different catalytic fields, but its structure has not been correctly reported so far. In this research, CeNiO$_3$ (RB1), CeO$_2$ and NiO have been synthesized in a nanocrystalline form using a modified citrate aqueous sol–gel route. A direct comparison between the equimolar physical mixture (n(CeO$_2$) : n(NiO) = 1 : 1) and compound RB1 was made. Their structural differences were investigated by laboratory powder X-ray diffraction (PXRD), selected area electron diffraction (SAED), transmission electron microscopy (TEM) with an energy-dispersive X-ray spectroscopy (EDS) detector, and Raman spectroscopy. The surface of the compounds was analyzed by X-ray photoelectron spectroscopy (XPS), while the thermal behaviour was explored by thermogravimetric analysis (TGA). Their magnetic properties were also investigated with the aim of exploring the differences between these two compounds. There were clear differences between the physical mixture of CeO$_2$ + NiO and RB1 presented by all of these employed methods. Synchrotron methods, such as atomic pair distribution function analysis (PDF), X-ray absorption near edge structure (XANES) and extended X-ray absorption fine structure (EXAFS), were used to explore the structure of RB1 in more detail. Three different models for the structural solution of RB1 were proposed. One structural solution proposes that RB1 is a single-phase pyrochlore compound (Ce$_2$Ni$_2$O$_7$) while the other two solutions suggest that RB1 is a two-phase system of either CeO$_2$ + NiO or Ce$_{1-x}$Ni$_x$O$_2$ and NiO.

Introduction

LnNiO$_3$ compounds (Ln – lanthanide cation) have already been investigated for different purposes, including electrocatalysis,[1] energy storage,[2,3] heterogeneous catalysis,[4,5] artificial intelligence,[6] gas sensing,[2] *etc*. Their metal-to-insulator transition has also been widely inspected.[7–17] In the previous literature,[9,18,19] it has been reported that LnNiO$_3$ compounds are distorted perovskites with defined crystallographic parameters. However, there are a lot of discrepancies in the literature concerning Ce-based compounds. Most of the recently published articles claim that they obtained phase pure CeNiO$_3$ compound which crystallizes as a perovskite-type oxide.[20–27] Nonetheless, the studies suffer from a lack of thorough physicochemical characterization, typically only showing powder X-ray analysis without providing any crystallographic information. Some authors tried to index the X-ray diffraction (XRD) pattern to the orthorhombic crystal system, space group *Pnma* with no detailed structural characterization.[20,21,26,27] Moreover, when comparing the XRD patterns given for CeNiO$_3$ with those of PrNiO$_3$[28,29] or other lanthanide nickelates,[30] clear differences in Bragg positions are observed, so there is no isostructurality.

In one study, it was claimed that CeNiO$_3$ was obtained using a citrate–nitrate combustion technique and provided

[a] Department of Chemistry, Josip Juraj Strossmayer University of Osijek, Cara Hadrijana 8/A, 31000 Osijek, Croatia. E-mail: igor.djerdj@kemija.unios.hr

[b] Department of Applied and Environmental Chemistry, University of Szeged, 6720 Szeged, Hungary

[c] University of Nova Gorica, Vipavska 13, 5000 Nova Gorica, Slovenia

[d] Institute Jožef Stefan, Jamova 39, 1000 Ljubljana, Slovenia

[e] Institute of Mathematics, Physics, and Mechanics, University of Ljubljana, Jamova 2, 1000 Ljubljana, Slovenia

[f] Faculty of Civil & Geodetic Engineering, University of Ljubljana, Jadranska 19, 1000 Ljubljana, Slovenia

[g] Surface Science Laboratory, Department of Materials and Earth Sciences, Technical University of Darmstadt, Otto-Berndt-Strasse 3, 64287 Darmstadt, Germany

[h] Institute of Crystallography, CNR, via Amendola 122/o, Bari 70126, Italy

† Electronic supplementary information (ESI) available. See DOI: https://doi.org/10.1039/d3dt03280a

Rietveld refinement data clearly showing a mixture of CeO_2 and NiO.[31] Detailed literature studies were conducted to find a crystallographic information file (.cif) to directly compare our experimentally obtained XRD pattern and to obtain crystallographic information but without success. Therefore, there is still no crystallographic proof of the existence of $CeNiO_3$ crystallizing in the perovskite structure.

Importantly, we noticed that what the literature claims to be the XRD pattern of the "$CeNiO_3$ perovskite" suspiciously has the same Bragg positions as the mixture of constituent oxides, fluorite CeO_2, and cubic NiO. There could be two explanations: either this is just a coincidence or $CeNiO_3$ is a mixture of CeO_2 and NiO at the nanoscale level.

Another possibility is that this "$CeNiO_3$" perovskite is a two-phase system containing solid solution $Ce_{1-x}Ni_xO_2$ and NiO. Various authors have investigated the Ni^{2+} doping effect of the CeO_2 structure.[32–39] These studies were mostly used for hydrogen production via water splitting[35] and as catalysts for the reduction of NO[40] or unsaturated organic compounds.[34,36,41] A similar application has also been reported for the "$CeNiO_3$" perovskite.[20,22–24,26]

Therefore, it is important to elucidate the actual structure of what the literature claims to be $CeNiO_3$ so that the structure–property relationship is established. If this is resolved, its properties could be improved by further research and consequently, its application. In this research, a compound that corresponds to $CeNiO_3$ (RB1) and the substituent oxides, CeO_2 and NiO, were synthesized in a nanocrystalline form by means of the previously developed modified aqueous sol–gel method.[42–48] Ceria and nickel oxide were mixed in an equimolar molar ratio ($n(CeO_2) : n(NiO) = 1 : 1$) after synthesis to obtain the same amounts of constituent oxides as there are in RB1, so the direct comparison between the physical mixture (CeO_2 + NiO) and a "compound" (RB1) can be made. Their structural features were thoroughly investigated using laboratory X-ray and electron diffraction, synchrotron, microscopic and spectroscopic methods, with the aim of solving the actual structure of RB1 ($CeNiO_3$). Their magnetic properties have also been explored to point out the differences in the synthesized compounds.

Experimental

Materials and methods

For the synthesis of materials, the following chemicals were used as presented in Table 1.

Table 1 List of chemicals used for the synthesis of Ce–Ni-based compounds

Chemical name	Manufacturer
Cerium(III) nitrate hexahydrate, 99.5%	Acros Organics, USA
Nickel nitrate hexahydrate, p.a.	T.T.T., Croatia
Citric acid monohydrate, Ph Eur	T.T.T., Croatia
Concentrated ammonia solution ($w = 25\%$), p.a.	Gram-Mol, Croatia

Chemicals were used as purchased, without further purification. MilliQ ultrapure water was obtained using a PURELAB Flex device for ultrapure water preparation. For pH value adjustment, a pH-meter HANNA pH 211 was used. The reaction solution was heated on a magnetic hotplate stirrer DLAB MS-H-S and dried in a drying oven Instrumentaria ST-01/02 afterwards. Calcination was performed in a muffle furnace Nabertherm LT5/11/B410.

Synthesis procedure

Stoichiometric amounts of metal cation precursors (see Table S1†) were dissolved in a 10% solution of citric acid in MilliQ water. Then, the pH value was adjusted to 5 using a concentrated ammonia solution. The as-prepared reaction solution was heated on a hotplate with constant stirring until a black resin was formed. The black resin was further dried at 120 °C overnight until it was completely solid. Finally, it was ground in a mortar and calcined in a furnace at 600 °C, heating rate 2 °C min⁻¹, and held at this temperature for 8 hours (stabilization time).

Characterization techniques

Powder X-ray diffraction. Powder XRD patterns in the range of $2\theta = 10°–100°$ were obtained using a PANalytical Aeris Research Diffractometer with CuKα radiation, step size 0.002°, 20.4 s per step. A divergence slit of 1° and a fixed mask of 13 mm were used in hardware settings.

Raman spectroscopy. Raman spectra were collected using a confocal microscope Sentera II, Bruker, 532 nm wavelength source, laser power 2.50 mW, spectral resolution 4 cm⁻¹, optical objective 50×, aperture 50 × 1000 μm, and 3 coadditions of 10 000 ms each measurement.

Transmission electron microscopy. For the observation, the sample was dispersed in absolute ethanol and dropcast on a carbon-coated copper grid. Transmission electron microscopy was performed using a JEOL JEM2100F equipped with a STEM unit and an EDS detector (Oxford Instruments). The acceleration voltage was 200 kV and the spot size in the STEM mode was 1 nm.

X-ray photoelectron spectroscopy. XPS spectra were collected using an integrated XPS system DAISY-BAT (Darmstadt's Integrated SYstem for BATtery Research). X-ray photoelectron spectroscopy (XPS) experiments were accomplished in a vacuum-cluster tool on a ULVAC-PHI VersaProbe II (part of DAISY-BAT) instrument with the base pressure in the analysis chamber below 5×10^{-9} mbar. Monochromatized Al Kα radiation (1486.6 eV) was utilized as the excitation source. Detailed spectra were recorded by applying a pass energy of 23.5 eV and a step size of 0.1 eV per step. Backgrounds of the acquired spectra were subtracted by using the Shirley method in CasaXPS, version 2.3.25.[49] Fitting of oxygen 1s components was performed by fitting with a GL(30) lineshape for all components and a fixed FWHM (full width at half maximum) for all components except the metal oxide.

Thermogravimetric analysis. TGA curves were recorded using a Mettler Toledo System 1 device. Alumina pans of 70 μL

were used. Prior to measurements of the sample, a blank curve was recorded with empty alumina pans. The method for sample measurement was adjusted to subtract the blank curve, a heating rate of 10 °C min⁻¹, gas flow (oxygen) of 200 mL min⁻¹.

X-ray absorption spectroscopy. The experiments were performed at the XAFS beamline of the ELETTRA synchrotron radiation facility in Trieste, Italy. A Si (111) double crystal monochromator was used with an energy resolution of about 0.7 eV at 7 keV. Higher harmonics were eliminated by detuning of the second monochromator crystal to 60% of the maximum in the rocking curve, and the size of the beam on the sample was set to about 1 mm × 5 mm. The intensity of the monochromatic X-ray beam was measured using three consecutive 30 cm long ionization detectors filled with optimal nitrogen, argon and helium gas mixtures for a given energy range, to obtain 15% absorption in the first cell, 70% in the second cell, and 90% in the second and third cells.

The samples were prepared in the form of homogeneous pellets, pressed from micronized powder mixed with micronized BN, with a total absorption thickness of about 1.5 above the Ni K-edge or Ce L_3-edge, and inserted in the monochromatic beam between the first two ionization detectors. The absorption spectra were measured in the energy region from −150 eV to +1000 eV relative to the Ni K-edge (8333 eV), while for the Ce L_3-edge (5724 eV) EXAFS scans were stopped at the Ce L_2-edge (6165 eV). Equidistant energy steps of 0.3 eV were used in the XANES region, while for the EXAFS region, equidistant k steps of 0.03 Å⁻¹ were adopted, with an integration time of 2 s per step. The exact energy calibration was established with simultaneous absorption measurement on 5 μm thick Ni metal foil for the Ni K-edge, or the CeO_2 reference sample (calibrated with vanadium metal foil) for the Ce L_3-edge, placed between the second and third ionization chambers. The energy reproducibility of the measured spectra was ±0.03 eV. The quantitative analysis of XANES and EXAFS spectra was performed using the Demeter (IFEFFIT) program package,[50] in combination with the FEFF6 program code for *ab initio* calculations of photoelectron scattering paths in quantitative EXAFS analysis.[51]

Atomic pair distribution function (PDF). The PDF profile of RB1 was recorded at the 28ID-2 beamline of the National Synchrotron Light Source (NSLS-II) of Brookhaven National Laboratory. Experimental conditions were an X-ray energy of 68.36 keV (λ = 0.1814 Å) and 0.5 mm × 0.5 mm beam size; the temperature on the sample was set to 80 K to enhance diffraction by reducing atomic thermal motion. A PerkinElmer XRD 1621 digital imaging detector having 2048 × 2048 pixels with 200 × 200 μm size was mounted orthogonal to the beam path at 206 mm downstream of the sample. Cerium oxide was measured as a standard material to calibrate the wavelength and detector position. An empty capillary was measured for background estimation, by using a statistic double that of the sample measurements. Diffraction images were azimuthally integrated and converted into intensity profiles *vs.* momentum transfer $Q = 4\pi \sin \vartheta/\lambda$ by using the DIOPTAS program.[52] PDF profiles were calculated from the background-subtracted Q profiles by using the PDFGetX3 program.[53] The parameters for PDF calculations (background subtraction, scale factor, minimum and maximum values of Q, degree of data-correction polynomial) were chosen to avoid large termination effects and preserve the signal-to-noise ratio. The Q_{max} value was 28.5 Å⁻¹. The PDF profile has been fitted with structural models by using the PDFGUI program.[54]

Magnetic property measurement. The magnetic properties of RB1 and input compounds CeO_2 and NiO were studied using a Quantum Design MPMS-XL-5 SQUID magnetometer. The static susceptibility of the sample was measured between 2 K to 300 K under a magnetic field of 1 kOe after zero-field cooling (ZFC) and field-cooling (FC) protocols. Isothermal magnetization curves M(H) were recorded at a temperature of 2 K between −50 kOe and 50 kOe.

Results and discussion

Structural and microstructural analysis

The studied literature[20–24,26,27] shows powder X-ray patterns that are similar to experimental XRD patterns shown in Fig. 1. However, a combination of XRD patterns of CeO_2 and NiO also gives the same XRD pattern that the literature[20–24,26,27] claims to be the $CeNiO_3$ perovskite. For this purpose, CeO_2 and NiO were synthesized separately by the same synthesis procedure as that used for RB1 ($CeNiO_3$) and were mixed in a mortar in an equimolar ratio ($n(CeO_2)$: $n(NiO)$ = 1 : 1). The results of the Rietveld refinement of RB1 and the CeO_2 + NiO mixture are given in Table 2.

Based on the literature, the actual structure of RB1 ($CeNiO_3$) is unknown, so we proposed three different possibilities:

(1) RB1 is an equimolar mixture of both cubic $Fm\bar{3}m$ CeO_2 and NiO.

(2) RB1 is a mixture of tetragonal $P4_2/nmc$ Ni-doped CeO_2 and cubic $Fm\bar{3}m$ NiO.

(3) RB1 is a novel cubic $Fd\bar{3}m$ compound with a pyrochlore structure and the chemical formula $Ce_2Ni_2O_7$.

The main challenge in a direct comparison of RB1 and previously reported $CeNiO_3$ is the lack of crystallographic data obtained by the Rietveld refinement in those research studies. The results presented in this study unequivocally indicate that our RB1 sample corresponds to the previously reported $CeNiO_3$. However, variations in synthesis procedures undoubtedly generate visible differences in structural features such as the degree of crystallinity. For instance, Harikrishnan *et al.*[21] employed a co-precipitation method using metal nitrates, NaOH, and potassium carbonate. After prolonged stirring of the solution followed by calcination at 650 °C, the targeted $CeNiO_3$ has been obtained. In another research conducted by the same author,[27] $CeNiO_3$ synthesis involved Ni-foam for active material growth, followed by autoclaving at 180 °C for 12 hours and then calcination at 600 °C under an inert (argon) atmosphere. These differences in synthesis approaches
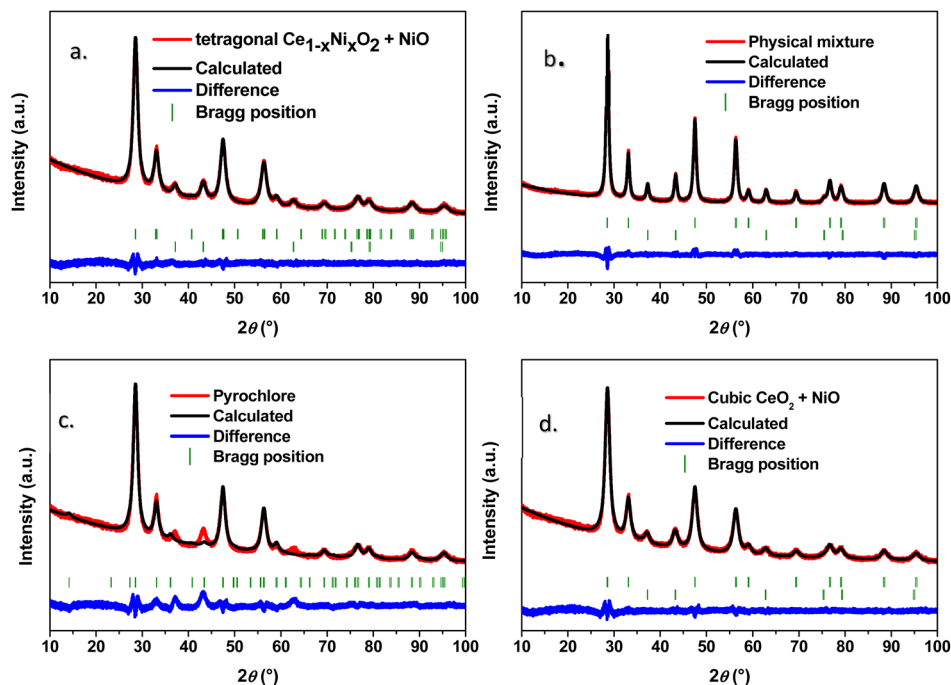
Fig. 1 Rietveld plots of (a) a structural solution of RB1 as a two-phase system: tetragonal solid solution $Ce_{1-x}Ni_xO_2$ + cubic NiO; (b) a refinement of the physical mixture of CeO_2 + NiO ($n:n = 1:1$) (c) a structural solution of RB1 as a single-phase pyrochlore $Ce_2Ni_2O_7$; (d) a structural solution of RB1 as a two-phase system: cubic CeO_2 + NiO. Red curves represent experimental patterns *versus* calculated patterns as black curves.

Table 2 Crystallographic information obtained from the Rietveld refinement of RB1 and a physical mixture of CeO_2 + NiO

Compound	RB1 (CeNiO₃)					CeO_2 + NiO ($n:n = 1:1$)	
	1		**2**		**3**		
Chemical formula	CeO_2	NiO	$Ce_{0.97}Ni_{0.03}O_2$	NiO	$Ce_2Ni_2O_7$	CeO_2	NiO
Crystal system	Cubic	Cubic	Tetragonal	Cubic	Cubic	Cubic	
Space group	$Fm\bar{3}m$		$P4_2/nmc$	$Fm\bar{3}m$	$Fd\bar{3}m$	$Fm\bar{3}m$	
Z	8		2	8	8	8	
Calculated density (g cm⁻³)	7.20	6.76	7.07	6.74	7.83	7.19	6.80
Unit cell parameters (Å)	5.4165(2)	4.1785(2)	a = 3.8208(3); c = 5.4492(2)	4.1903(2)	10.8406(9)	5.4162(2)	4.1861(2)
Unit cell volume (Å³)	158.88(6)	73.36(1)	79.55(1)	73.57(1)	1273.98(8)	158.91(6)	72.96(1)
Phase content (wt%)	71.0(2)	29.0(3)	71.34(1)	28.66(4)	100(4)	66.73(2)	33.27(2)
Average crystallite size (nm)	5.1	4.6	5.2	4.7	5.4	9.6	9.8
Average apparent microstrain (×10⁻⁴)	0.95		0.95		4.47	0.95	
R_B	0.91	1.02	0.88	0.75	4.40	1.45	0.68
R_P, R_{wp}, R_e	10.9, 9.19, 8.08		11.0, 9.21, 8.13		19.9, 17.9, 8.59	9.87, 8.44, 6.56	
χ^2	1.29		1.28		4.32	1.66	

affected only the degree of crystallinity, whilst the positions of Bragg reflections of the claimed CeNiO₃ and their relative intensities are almost intact. Our initial goal was to directly compare the equimolar physical mixture of CeO_2 + NiO ($n(CeO_2):n(NiO)$ = 1:1) and RB1 prepared under the same synthesis conditions to identify potential differences in the crystallographic structure. Here, we assumed that RB1 consists of both cubic CeO_2 and NiO, so the physical mixture of these two constituent oxides should not differ much from RB1. As for the unit cell parameters and crystal structure, these two samples appear to be the same. However, the phase content slightly differs since there is around

4 wt% more of CeO_2 in RB1. Also, there is a large difference in average crystallite size values. The refinement of the physical mixture of CeO_2 + NiO reveals crystallite sizes of constituent oxides that are two times larger than those found in RB1. This can be directly seen from the broadened Bragg peaks of RB1 compared to the physical mixture.

Another possibility was that cerium and nickel form a unique single-phase compound. For the proposal of an actual crystal structure of RB1, we have tried to solve it *ab initio* from the powder XRD pattern. However, this is a complex task since there are only a few broad peaks present, so our attempt was

unsuccessful. Therefore, we have tried to find XRD patterns of different compounds in the literature that are similar to the experimental XRD pattern of RB1. The most suitable XRD pattern that was found was that of pyrochlore $Ce_2Zr_2O_7$[55] which was used as a starting point. However, the content of the unit cell was changed to refine it with the obtained XRD pattern of RB1. Although this refinement appears to be correct, the plot given in Fig. 1c demonstrates that there are slight differences in the peak positions between the calculated and experimental patterns.

Mahammadunnisa et al.[32] investigated the impact of doping CeO_2 with 5–30 wt% of Ni^{2+}. In their synthesis procedure, specific amounts of metal nitrates and citric acid were dissolved in distilled water, sonicated, and placed in a pre-heated furnace at around 450 °C, causing a spark, leading to the formation of a solid product. The samples further underwent calcination at 600 °C for 4 hours to eliminate the carbon content. They have noticed that there is a slight decrease in unit cell parameters due to doping CeO_2 with a smaller cation Ni^{2+} (C.N. = 6, $r = 0.69$ Å (ref. 56)) in NiO, compared to Ce^{4+} (C.N. = 8, $r = 0.97$ Å (ref. 56)) in CeO_2, which is also visible in RB1 compared to the physical mixture of constituent oxides (CeO_2 + NiO). Two additional peaks in the XRD pattern of Ce–Ni–O systems[32] at $2\theta = 37°$ and $2\theta = 43°$ correspond to the NiO phase and only appear when doping of CeO_2 is beyond 15 wt%. Zhou et al.[57] used three types of synthesis procedures, all including metal nitrates as the starting material: (i) the citrate acid method by adding citric acid into the nitrate aqueous solution, heating until gel was formed and then calcination at 450 °C; (ii) the coprecipitation method with addition of potassium carbonate, followed by the adjustment of the pH value and then calcination at 450 °C, and (iii) the ammonia evaporation method, which included addition of NH_3 to aqueous solution of metal nitrates until a specific pH value, followed by calcination at 450 °C. They have shown that Ni-loading in ceria must be beyond 20 mol% for these additional peaks to appear. Therefore, the NiO phase detected by XRD in RB1 might be the NiO that is dispersed on the surface of ceria, while the rest of it could be dissolved in the cerium-nickel-based tetragonal solid solution $Ce_{1-x}Ni_xO_{2-\delta}$.[57] Another difference between the physical mixture of CeO_2 + NiO and RB1 is in average crystallite size values which can also be estimated from the Bragg peak widths on X-ray diffraction patterns (Fig. 1a compared to Fig. 1b). In the physical mixture CeO_2 + NiO, the average crystallite sizes of the constituent oxides are twice as large as those in RB1 (Table 2). Mahammadunisa et al.[32] also reported this behaviour as an effect of doping CeO_2 with NiO. They attributed it to the incorporation of nickel cations in the initial structure of ceria.[58] Even though these authors did not refine the XRD patterns they obtained, it was probably assumed that both $Ce_{1-x}Ni_xO_{2-\delta}$ and NiO are cubic, at least according to the given results. Small dopant concentrations can still preserve the cubic crystal structure of ceria.[59] However, doping ceria with other elements can also result in symmetry breaking from the cubic to the tetragonal crystal structure, which cannot be detected by XRD.[5,60,61]

Another method that is sensitive to phase formation and therefore useful for distinction between cubic and tetragonal crystal structures is Raman spectroscopy. Therefore, the Raman spectra of RB1 and a physical mixture of CeO_2 + NiO were recorded in the range from 1200 cm^{-1} to 80 cm^{-1} at an excitation wavelength of 532 nm and are shown in Fig. 2. According to Kroumova et al.,[62] CeO_2 with a fluorite structure should possess only one Raman active mode, T_{2g}, also known in the available literature as the F_{2g} vibration.[43] However, cubic NiO has no Raman active modes.[62] Therefore, the Raman spectrum of the physical mixture of CeO_2 and NiO should contain only one Raman active mode corresponding to fluorite ceria, as shown in Fig. 2 (red). Sole NiO would not be visible in the Raman spectrum. A strong F_{2g} vibration of CeO_2 in the Raman spectrum of the physical mixture CeO_2 + NiO is found at 450 cm^{-1}. The Raman spectrum of RB1 shows a strong peak slightly shifted to higher wavenumbers, at 455 cm^{-1}. Also, an additional defect peak at 576 cm^{-1} coincides with the vibrations that are often assigned to oxygen vacancies in CeO_2-based compounds.[48,59,63–67]

Cop et al.[59] have shown that doping ceria with different cations results in the appearance of additional defect bands that are a result of increased concentration of oxygen vacancies. Various other authors have shown that these bands are expected when CeO_2 is doped with other cations,[32,59,68] especially when these cations are aliovalent,[59] such as Ni^{2+}. Also, a peak at 220 cm^{-1} is not active in the fluorite-structured ceria. This phonon mode is often activated in doped ceria, especially if there is a mismatch in ionic radii and ionic charge of dopants.[61,69] Therefore, a tetragonal solid solution would explain the symmetry breaking observed in the Raman spectrum of RB1. Popović et al.[38] have investigated charge delocalization in ceria upon doping with $Fe^{2+/3+}$. They observed that the doping of ceria with smaller cations has an impact on the position of F_{2g} mode because of the shrinkage of the unit cell. Also, charge mismatch and the small crystallite size impact oxygen vacancy concentration and the intensity of the vacancy mode.[38] Atzori et al.[70] have also investigated CeO_2–
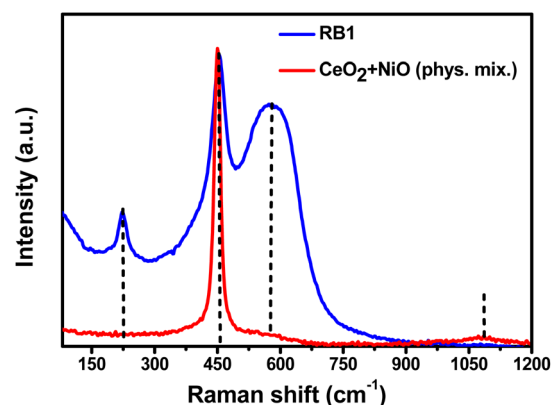

Fig. 2 Raman spectra of the RB1 sample and physical mixture of cerium(IV) and nickel(II) oxide (1 : 1).

NiO systems synthesized using the surface-templated method with direct synthesis of metal oxides from nitrates, dissolved in water with the template and NaOH, then filtered and calcined to obtain the targeted compound. Another used route was the synthesis of CeO_2 while Ni was deposited through incipient wetness impregnation technique. They have shown that this large defect band increases with increased Ni loading. Several other authors have studied $Ce_{1-x}Ni_xO_{2-\delta}$ for various catalytic applications.[33,41,71,72] Barrio *et al.*[33] even reported that the limit of the solubility of Ni in ceria ranges from 10 to 12 mol%, even though they did not give information on the $Ce_{1-x}Ni_xO_{2-\delta}$ unit cell content. These values were calculated from the difference in the NiO content; they assumed that the remaining Ni was dissolved in CeO_2. The total Ni-content in RB1 is 30 wt%, which is 50 mol%, but there is only 3 mol% of total Ni-content dissolved in the tetragonal solid solution in our case according to the Rietveld refinement results. It seems that in our case, there is much less Ni that is dissolved in CeO_2, but none of the mentioned research papers calculated the actual amount of Ni dissolved in the solid solution directly from the unit cell content. Therefore, we must consider their results carefully.

Additionally, it was necessary to record Raman spectra of CeO_2 and NiO separately, to further inspect their structure. Fig. 3a and b shows individual Raman spectra of CeO_2 and NiO. The Raman spectrum of pure CeO_2 shows typical strong F_{2g} vibration at 462 cm^{-1} and a wide defect peak from 550–650 cm^{-1} that occurs due to the presence of oxygen vacancies.[73] Now, it can be observed that F_{2g} vibration is red-shifted in both RB1 and the CeO_2 + NiO mixture. Also, the NiO spectrum reveals a low-intensity wide peak at 506 cm^{-1} that cannot be classified as Raman-active mode since its intensity is 150 times lower than the intensity of F_{2g} vibration in CeO_2. Also, there are two additional broad peaks at around 190 cm^{-1} and 1075 cm^{-1}, with even lower intensity. The inset in Fig. 3b shows the Raman spectrum of NiO on the same scale as the CeO_2 spectrum in Fig. 3a to visualize the difference in intensities and thus to explain the absence of these peaks in the Raman spectrum of the CeO_2 + NiO mixture. According to George *et al.*[74] these peaks appear due to the first- and second-order Raman scattering in NiO-nanostructures because of the structural defects. To conclude, there is a clear difference between RB1 and the CeO_2 + NiO mixture in terms of Raman spectroscopy.

Nevertheless, additional analyses are necessary to resolve this structural issue. One of them is transmission electron microscopy. Fig. 4 and 5 show STEM, TEM, and SAED images of RB1. STEM-EDS mapping in Fig. 4 shows a uniform distribution of involved cations in RB1. The physical mixture of CeO_2 + NiO does not have a uniform distribution of cerium and nickel, as shown in Fig. S1 and S2 in the ESI.† This is a difference that can have an impact on the difference in catalytic activity or some other physical properties.

TEM, HRTEM and SAED images confirm the nanocrystalline nature of synthesized RB1. The crystallite size values nearly correspond to the ones calculated by the Rietveld refinement of the XRD pattern of RB1. Measured interplanar distances (d values) were compared to values obtained from the Rietveld refinement results of RB1 for three different cases. A comparison is given in Table 3.

As seen in Table 3, the cubic $Fm\bar{3}m$ crystal structure can be ruled out due to the missing interplanar distance. Therefore, the actual compound present in RB1 could be in the form of a solid solution $Ce_{1-x}Ni_xO_2$, or it could crystalize as a pyrochlore $Ce_2Ni_2O_7$.

Normalized Ni K-edge XANES spectra recorded for nanocrystalline NiO and RB1 are shown in Fig. 6, together with the spectra of the corresponding crystalline NiO reference compound. The energy position of the Ni K-edge and the edge profile in NiO and RB1 coincide with the energy position and edge profile of crystalline NiO with Ni in the 2+ state. This shows that the valence state and local symmetry of Ni cations is the same as in the crystalline NiO. Ni K-edge EXAFS analysis is used to detect the average local environment of Ni cations in the nanocrystalline NiO and RB1 samples. In the Fourier transform (FT), the magnitude of the k^3-weighted EXAFS spectra are plotted in Fig. 7. The contributions of photoelectron scattering on the nearest shells of neighbours around the Ni atoms are observed in the R range of up to about 6 Å. Already by qualitative comparison of the FT EXAFS spectra, it is evident that both

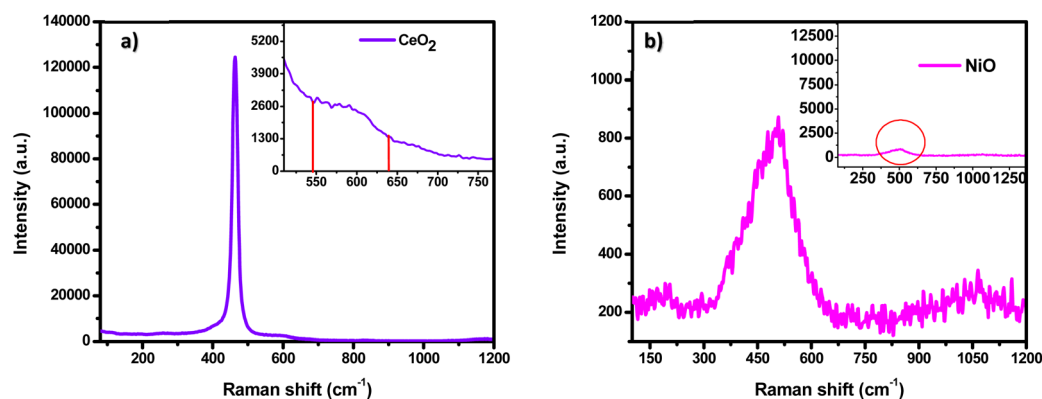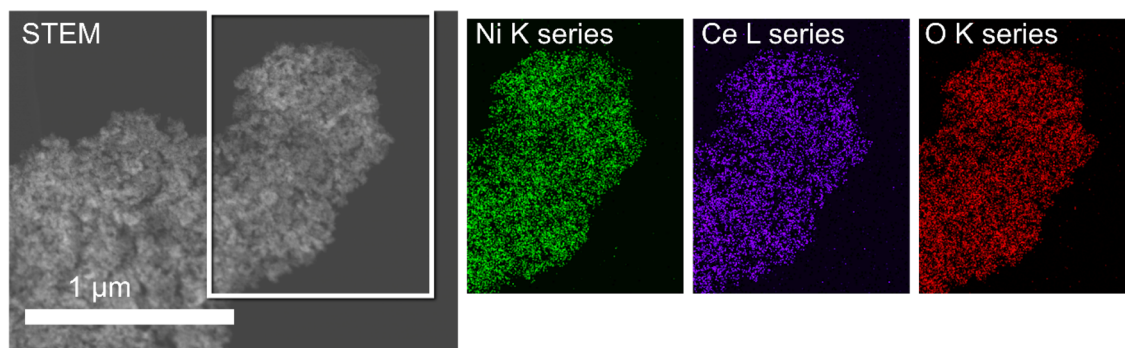**Fig. 3** Raman spectrum of (a) CeO_2 and (b) NiO.

Fig. 4 STEM-EDS mapping of RB1 ($CeNiO_3$) nanoparticles agglomerate.

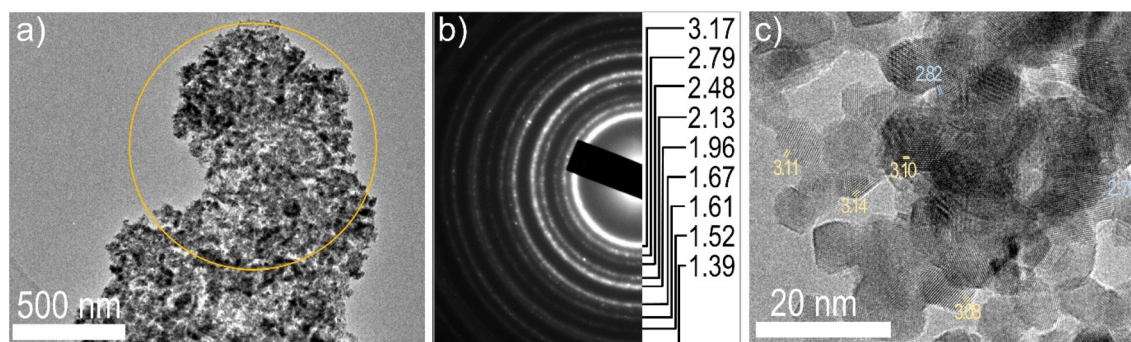**Fig. 5** (a) TEM image of RB1 ($CeNiO_3$) nanoparticle agglomerate and (b) a corresponding SAED with assigned *d*-values in Å. (c) HRTEM of RB1 ($CeNiO_3$) nanoparticles, *d*-values in Å.

Table 3 Comparison of calculated interplanar distances (*d*) of RB1 obtained from SAED pattern with the Rietveld refinement results for three different crystal structures (cubic, tetragonal, pyrochlore) with assigned Miller indices (*hkl*) for each crystal structure

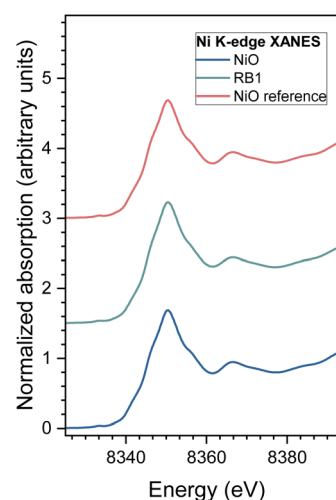|	Rietveld refinement					
	Cubic $Fm\bar{3}m$		Tetragonal $P4_2/nmc$		Cubic pyrochlore $Fd\bar{3}m$	
SAED pattern	*d* (Å)	*hkl*	*d* (Å)	*hkl*	*d* (Å)	*hkl*
3.17	3.13	111	3.13	101	3.13	222
2.79	2.71	200	2.72	002	2.71	400
2.48	2.41	111	2.42	111	2.49	331
2.13	2.09	200	2.10	200	2.09	511
1.96	1.92	220	1.92	112	1.92	440
1.67	—	—	1.64	103	1.65	533
1.61	1.63	311	1.63	211	1.63	622
1.52	1.56	222	1.56	202	1.52	551
1.39	1.35	400	1.36	004	1.36	800

Fig. 6 Ni K-edge XANES spectrum of nanocrystalline NiO and RB1 samples with the crystalline NiO reference compound. Spectra are shifted vertically for clarity.

samples exhibit the same Ni local structure characteristic of crystalline NiO with an FCC crystal structure, as in the crystalline NiO reference.[75] Quantitative EXAFS analysis is used to determine the structural parameters of the average local Ni neighbourhood (the type and average number of neighbours; the radii and Debye–Waller factor of neighbouring shells) in

the samples. The structural parameters are quantitatively resolved from the EXAFS spectra by comparing the measured EXAFS signal with the model signal. The FEFF model for the crystalline NiO nanoparticles is based on the cubic crystal structure of NiO with the space group $Fm\bar{3}m$ with the lattice
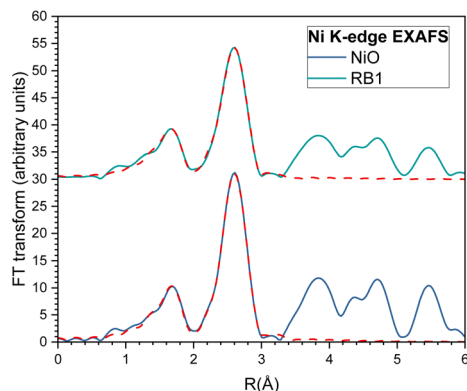
Fig. 7 Fourier transform magnitude of the k^3-weighted Ni K-edge EXAFS spectra of the nanocrystalline NiO and RB1 samples, calculated in the k range of 3–12 Å. Experiment − (solid line); the best fit EXAFS model calculated in the R-range of 1.2 to 3.3 Å − (red dashed line). Graph curves are shifted vertically for clarity.

Table 4 Parameters of the nearest coordination shells around Ni cations in the NiO and RB1 samples: coordination number (N), distance (R), and Debye−Waller factor (σ^2). Uncertainty of the last digit is given in parentheses. The best fit is obtained with the amplitude reduction factor $S_0^2 = 0.9$ and the shift of the energy origin $\Delta E_o = -2.7(4)$ eV

Neighbour	N	R (Å)	σ^2 (Å²)	R-factor
NiO				
O	6.0(5)	2.079(4)	0.0052(7)	0.00086
Ni	12.0(5)	2.953(2)	0.0058(2)	
O	8.0(5)	3.46(3)	0.010(7)	
RB1				
O	6.1(5)	2.074(4)	0.0061(8)	0.0019
Ni	11.0(7)	2.957(3)	0.0067(3)	
O	7.3(4)	3.46(2)	0.010(3)	

constant $a = 4.177$ Å,[76] where Ni is coordinated with 6 oxygen atoms at a distance of 2.09 Å, 12 Ni atoms at 2.95 Å and 8 oxygen atoms at 3.62 Å.
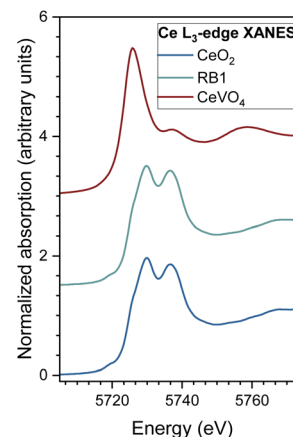
The FEFF model comprised three single scattering and two significant multiple scattering paths up to 3.6 Å, with 8 variable parameters: coordination shell distance (R) and Debye–Waller factors (σ^2) of all single scattering paths, and the amplitude reduction factor (S_0^2) and shift of the energy origin of the photoelectron (ΔE_o), common to all scattering paths, are introduced. The structural parameters of multiple scattering paths are constrained to those of the corresponding single scattering paths. The model was tested on the EXAFS spectrum measured for the crystalline NiO.[75] The same FEFF model is used in the fit of the EXAFS spectra of the nanocrystalline NiO and RB1 samples, but here, the amplitude reduction factor (S_0^2) was fixed to a value of 0.90 obtained for the crystalline NiO, and the shell coordination numbers were used as variable parameters. A very good EXAFS fit (Fig. 7) is obtained in the k range of 3–12 Å and the R-range of 1.2–3.3 Å. The best-fit structural parameters are given in Table 4. The results show that the local structure around Ni cations in the nanocrystalline RB1 sample is the same as that in the nanocrystalline NiO compound. The structural parameters of the RB1 sample are the same as those of the nanocrystalline NiO sample, except that the Debye–Waller factors are slightly larger in RB1, indicating a larger structural disorder in the crystalline structure.

To test for the eventual presence of the RB1 nanocrystalline structure one single scattering path from Ce neighbours is added to the FEFF model at the distance characteristic for Ni–Ce in the RB1 crystal structure. The presence of Ce neighbour in the local neighbourhood around Ni cations is excluded by the fit, showing there is no presence of Ce in Ni neighbourhood or it is below the detection limit.

Normalized Ce L_3-edge XANES spectra measured on CeO_2 and RB1 are shown in Fig. 8, together with the spectra of the corresponding Ce^{3+} reference compounds (crystalline $CeVO_4$).[77]


Fig. 8 Ce L_3-edge XANES spectra of CeO_2 and RB1 samples, and $CeVO_4$ as a reference for Ce^{3+}.

The energy position of the Ce L_3-edge and the edge profile in RB1 completely coincide with the energy position and edge profile of CeO_2, indicating that all Ce cations in the sample are in the Ce^{4+} valence state. If the sample contains a mixture of two or more compounds of the same cation with different local structures and valence states, the measured XANES spectrum is a linear combination of individual XANES spectra of different cation sites. In such cases, the relative amounts of the cation at each site and the average valence state of the cation in the sample can be determined by the linear combination fit (LCF) with XANES spectra. LCF analysis of the XANES spectra on RB1 with the XANES spectra of the reference compounds (CeO_2 as reference for Ce^{4+}, and $CeVO_4$ as reference for Ce^{3+}) shows that there is no significant presence of Ce^{3+} species. Quantitative EXAFS analysis to determine the structural parameters of the average local Ce neighbourhood was carried out for CeO_2 and RB1 samples (see ESI, Fig. S3 and Table S2†). The structural parameters for RB1 are quantitatively and equally well resolved from the EXAFS spectra using the FEFF models for CeO_2 with a cubic ($Fm\bar{3}m$) and tetragonal ($P4_2/nmc$) structure. This shows that EXAFS cannot resolve between cubic and tetragonal structures for the RB1 sample.
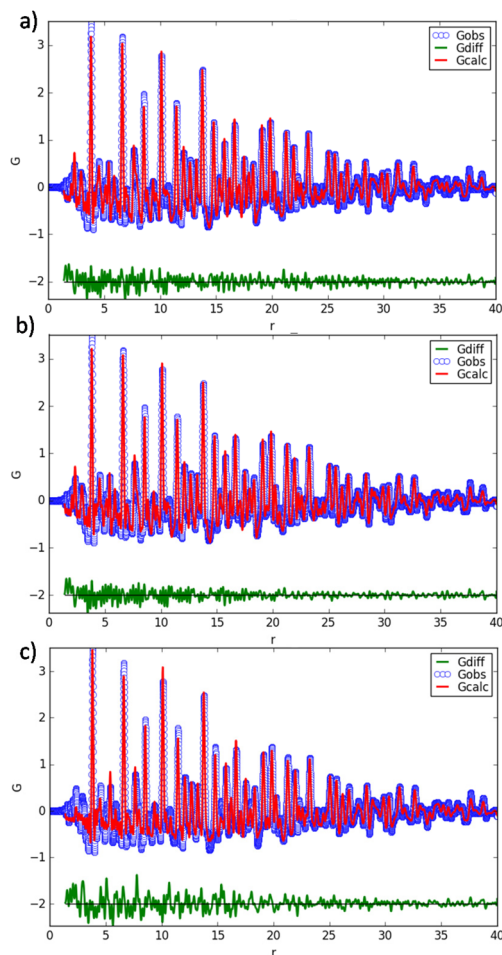
Fig. 9 Fit of the PDF profile of RB1 (experimental data = blue circles, fit curves = red line, residuals = green line) by using a structural model obtained by combining (a) cubic $Fm\bar{3}m$ CeO$_2$ and NiO, (b) tetragonal $P4_2/nmc$ Ni-doped CeO$_2$ and cubic $Fm\bar{3}m$ NiO and (c) a hypothetical cubic $Fd\bar{3}m$ compound with a pyrochlore structure and the chemical formula Ce$_2$Ni$_2$O$_7$.

The obtained structural parameters for RB1 are in agreement with those obtained for pure CeO$_2$ (Table S2†).

The atomic pair distribution function (PDF) profile of RB1 has been fitted to test the three modelling hypotheses. The crystal cell parameters and atomic displacement parameters and positions not constrained by symmetry have been refined for all the crystal phases. Results are shown in Fig. 9, while the main fitting parameters are reported in Table 5. It can be noted that the hypothesized pyrochlore structure is ruled out by the poorer PDF fitting, as the corresponding calculated profile shows significant differences compared to the observed one even at small interatomic distances (Fig. 9c). For the remaining structural hypotheses (1) and (2) there is an overall agreement with reciprocal space determinations (Rietveld analysis) for crystal cell and weight fraction parameters, and the average crystallite size is in good agreement with the particle diameter estimated by PDF (SP$_{diameter}$). However, PDF data definitively resolves the question of which structural description is the best among the two linear combinations of crystal phases. A better fit is achieved when the cubic NiO crystal phase is coupled with the tetragonal Ni-doped CeO$_2$ rather than the cubic CeO$_2$ one. In the latter case, a weight agreement factor $R_w = 0.163$ is obtained and the observed-calculated difference profile in Fig. 9b only contains only high-frequency noise throughout the profile.

Additionally, X-ray photoelectron spectroscopy (XPS) was conducted to investigate the surface of the materials. XPS spectra were recorded for NiO and CeO$_2$ separately and for all synthesized compounds. Fig. 10 shows high-resolution Ce 3d spectra for CeO$_2$ and RB1, respectively. The Ce 3d spectrum of CeO$_2$ shows the typical 3d$_{5/2}$ at 883.1 eV and the 3d$_{3/2}$ at 901.7 eV with a spin–orbit splitting of 18.6 eV. The spectra exhibit strong charge-transfer satellites[78,79] and additional overlapping peaks from multiplet effects.[80] The position and intensity ratio between those peaks depends on the oxidation state, the ligand type, and the next-nearest neighbour.[80] This makes analysing core spectra of mixed transition metal and lanthanide oxides difficult. It was pointed out[81] that satellites 3 and 4 can be directly related to cerium 4+ (CeO$_2$), which shows that both

Table 5 Parameters determined by fitting the PDF profile of RB1 with a structural model composed of a combination of cubic $Fm\bar{3}m$ CeO$_2$ and NiO (1), tetragonal $P4_2/nmc$ Ni-doped CeO$_2$ and cubic $Fm\bar{3}m$ NiO (2) and a hypothetical cubic $Fd\bar{3}m$ compound with a pyrochlore structure and chemical formula Ce$_2$Ni$_2$O$_7$ (3). R_w is the weighted agreement factor between observed and calculated PDF, Q_{broad} describes the peak broadening from increased intensity noise at high Q, scale is an overall scale factor, δ_1 is the coefficient for $1/r$ contribution to the peak sharpening, SP$_{diameter}$ is the particle diameter for the PDF shape damping function

	1		**2**		**3**
Chemical formula	CeO$_2$	NiO	Ce$_{0.97}$Ni$_{0.03}$O$_2$	NiO	Ce$_2$Ni$_2$O$_7$
Crystal system	Cubic	Tetragonal	Cubic	Cubic	
Space group	$Fm\bar{3}m$	$P4_2/nmc$	$Fm\bar{3}m$	$Fd\bar{3}m$	
Fit range	1.4–40.0 Å		1.4–40.0 Å		1.4–40.0 Å
R_w	0.193		0.163		0.261
Q_{broad}	0.040		0.028		0.040
Scale	0.136		0.141		0.08
Phase content (wt%)	76.9	23.1	77.0	23.0	100
δ_1	2.07	1.50	2.10	1.54	2.44
Unit cell parameters (Å)	5.402	4.175	$a = 3.812$; $c = 5.417$	4.175	10.804
SP$_{diameter}$ (nm)	5.5	5.2	5.4	5.0	5.7

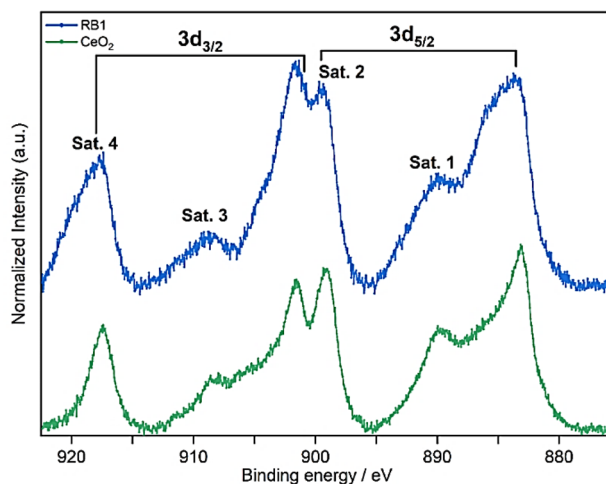**Fig. 10** High-resolution Ce 3d spectra of CeO₂ and RB1.

Fig. 11 High-resolution Ni 2p XPS spectra of NiO and RB1.

materials in Fig. 10 mainly consist of cerium 4+. However, the CeO₂ deviates from PLD-deposited films shown in ref. 81 indicating that cerium 3+ is present on the surface, which could be due to the formation of cerium hydroxide, clearly seen in the O 1s spectra (Fig. S4b†).

In the Ce 3d spectra of RB1, the left shoulder of the $3d_{5/2}$ main peak broadens while the $3d_{3/2}$ main peak increases in intensity, which indicates the higher cerium 3+ content in RB1 compared to the CeO₂ sample. This could hint at a mixed oxidation state of cerium and nickel or an oxygen-deficient structure. However, in the O 1s spectra of RB1 (Fig. S4c†), the cerium hydroxide content on the surface is high, which would result in cerium in the 3+ state. Reference spectra without the influence of hydroxide could be used in the fitting procedure to analyze the content of different cerium components. Peak position analysis is summarized in Table S3.†

Similar analysis was performed for the high-resolution Ni 2p spectra, in order to investigate the stoichiometry of the compounds and the oxidation state of nickel cations in both samples. The Ni 2p spectra are shown in Fig. 11 for NiO and RB1 and the peak position analysis is summarized in Table S4.†

The Ni 2p spectrum of NiO shows $2p_{3/2}$ (853.0 eV) and $2p_{1/2}$ (871.5 eV) doublets with a spin–orbit splitting of 17.5 eV.[82] The core level peaks at 856.1 and 873.2 eV are a sign of the presence of non-stoichiometry in NiO and the existence of Ni³⁺, respectively.[82,83] It has been previously reported that satellite peaks 2 and 3 also point out towards the existence of Ni³⁺.[83,84] Nickel oxide prepared at lower temperatures (>700 °C) has a higher concentration of Ni³⁺ than Ni²⁺.[82,85] Interestingly, a fully stoichiometric NiO compound is formed after calcination at 1100 °C.

The explanation of the nonstoichiometry in nanocrystalline nickel oxide lies in the formation of Ni²⁺ vacancies[85,86] because of excess oxygen. Positively charged nickel-vacant holes (h⁺⁺) are typically neutralized by receiving two electrons from the neighbouring Ni²⁺ species, causing them to increase
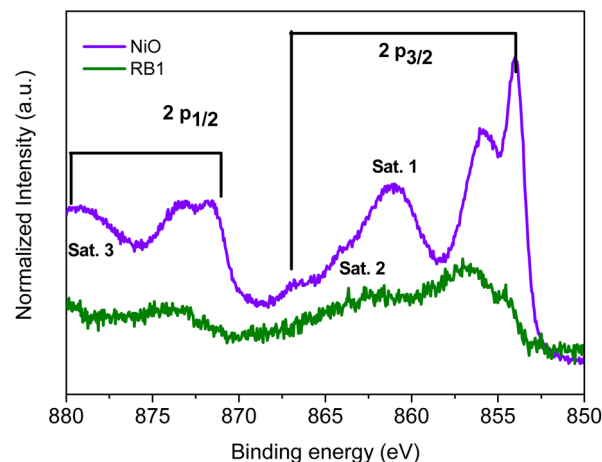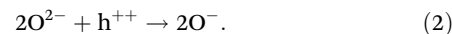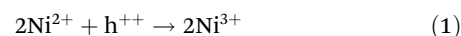
their oxidation state to Ni³⁺. In addition, there is another possible way of neutralizing the charge mismatch by neighbouring O²⁻ species, thus creating reactive electrophilic O⁻ species.[85,87] These reactions are summarized in eqn (1) and (2):

$$2Ni^{2+} + h^{++} \rightarrow 2Ni^{3+} \tag{1}$$

$$2O^{2-} + h^{++} \rightarrow 2O^{-}. \tag{2}$$

The electrophilic oxygen species are ideal candidates for nucleophilic attack by hydroxide or water thus making them highly active in the formation of O–O bonds.[87] Therefore, they are very important for the oxygen evolution reaction (OER).[88–90] However, electrophilic oxygen can also be used for the reduction of unsaturated organic compounds.[34,36,41]

When comparing the Ni 2p spectrum of NiO and RB1, one can see that the RB1 spectrum is very noisy and cannot be interpreted easily. This is probably due to the interference of the charge-transfer satellite peaks in the Ni 2p region with the Ce 3d region in RB1.[91] However, there is a sign of core level peaks at 854 and 856 eV, where the peak at 856 is higher in intensity and broadened compared to the peak at 854 which could indicate a higher content of Ni³⁺ in RB1 than in pure NiO. This could be due to the higher hydroxide content on the surface of RB1 and the formation of NiOOH, as seen in the high-resolution O 1s spectra shown in Fig. S4.†

All O 1s spectra in Fig. S4† show a lattice oxygen (O_L) peak at 530 eV. While the NiO and CeO₂ spectra show two additional peaks at 531 eV and 533 eV. The peak at 531 eV can be related to loosely bound/adsorbed surface oxygen species (O_ads), while the peak at around 533 eV is ascribed to adsorbed OH-groups or water molecules (O_OH), in good agreement with the literature.[85,88,92] The deconvolution parameters of O 1s spectra are summarized in Table S5 (ESI).† NiO and CeO₂ have a similar concentration of adsorbed oxygen species (around 30%), while RB1 contains almost 67% of adsorbed hydroxide groups. This could be attributed to the almost two times smaller crystallite size of RB1, providing substantially more surface area for oxygen species to adsorb at.

The results of thermogravimetric analysis (Fig. S5†) can also confirm the presence of higher content of Ni^{3+} and Ce^{3+} in RB1 than in a physical mixture of constituent oxides since there is a higher oxygen uptake in RB1. During heating in an oxidative atmosphere, Ce^{3+} is oxidized to Ce^{4+}, while the surface hydroxides are removed. However, heating non-stoichiometric Ni-based oxides increases stoichiometry and thus decreases the concentration of nickel vacancies.[82]

To further corroborate our structural findings, aiming to clarify the earlier assumption that RB1 is $CeNiO_3$ or not, we have synthesized an additional compound $Ce_{0.97}Ni_{0.03}O_2$ and conducted several additional measurements (PXRD and Raman spectroscopy). These additional measurements prove that, indeed, the equimolar introduction of Ni into the CeO_2 lattice does not yield the single $CeNiO_3$ compound. Instead, it likely forms a mixture with two distinct phases: $Ce_{1-x}Ni_xO_2$ and NiO. The synthesis of 3% Ni-doped CeO_2 yielded phase-pure, tetragonal $Ce_{0.97}Ni_{0.03}O_2$, which agrees well with crystallographic data reported for RB1. Rietveld refinement results presented in Fig. 12a and Table S6† confirmed almost identical values for this compound compared to the phases reported for RB1 in Table 2.

In addition to that, Raman spectroscopy measurements were employed to provide a further proof (Fig. 12b). The defect peak at 576 cm^{-1} decreased proportionally with the reduction in Ni-dopant concentration, aligning with the 50% dopant level in RB1 and the 3% Ni-doped sample. Moreover, a consistent increase in the CeO_2 Raman active mode intensity (F_{2g} at 450 cm^{-1}) occurred with decreasing dopant content. Additionally, the intensity evident at 220 cm^{-1} suggests Ni integration into CeO_2 as in the RB1 compound.

Magnetic properties

Since nickel is one of the elements of the iron triad group, nickel-based compounds are known as magnetically active compounds. Therefore, magnetic measurements of RB1 ($CeNiO_3$) and a physical mixture of CeO_2 + NiO should also give an insight into a possible difference between the properties of these compounds. Fig. 13a shows a temperature-dependent susceptibility of two input compounds and RB1. The measured negative susceptibility of CeO_2 above 50 K means that the compound is a diamagnet at room temperature. The result is consistent with the expected nonmagnetic

Ce^{4+} ion in CeO_2. Only below 50 K a week paramagnetic signal appears ($1/T$ dependence of the susceptibility), which can be attributed to lattice defects or oxygen vacancies.[93,94] The isothermal magnetization at 2 K (Fig. 13b) can be described as a sum of paramagnetic and diamagnetic contributions. The maximal value at 50 kOe is as small as 0.033 emu g^{-1}. We can conclude that the magnetic signal of CeO_2 is much smaller than the magnetic signals of NiO and RB1. Bulk NiO is an antiferromagnet with the Néel temperature of 523 K.[95] The almost temperature-constant susceptibility and linear magnetization curve at 2 K of NiO nanoparticles that were used as the input material in the synthesis, are consistent with the antiferromagnetic order of NiO. Weak splitting of zero-field cooled (ZFC) and field cooled (FC) susceptibilities and tiny hysteresis in $M(H)$ are due to uncompensated magnetic moments on the surface of the nanoparticles.[96]

The magnetic behaviour of the newly synthesised compounds RB1 and CeO_2 (3% doped Ni) differ significantly from the magnetic properties of CeO_2 and NiO nanoparticles. A much larger splitting between ZFC and FC susceptibility and hysteresis with a coercive magnetic field of 600 Oe and a remanent magnetization of 0.02 emu g^{-1}, are clear evidence of a ferromagnetic order in $CeNiO_3$ (RB1). The local maximum of ZFC susceptibility at about 100 K and the temperature at which the ZFC and FC curves diverge (about 220 K) are quite different, indicating a rather broad size distribution of RB1 nanoparticles. The temperature where ZFC and FC curves diverge shifts to lower temperatures in CeO_2 (3% doped Ni) while the isothermal magnetization at 2 K of only 3% doped CeO_2 is already quite similar to the $M(H)$ curve of RB1. These results support the finding that RB1 is the mixture of $Ce_{0.97}Ni_{0.03}O_2$ and NiO. Several publications have reported on the ferromagnetism of $Ce_{1-x}Ni_xO_2$ nanoparticles.[97–101] In our
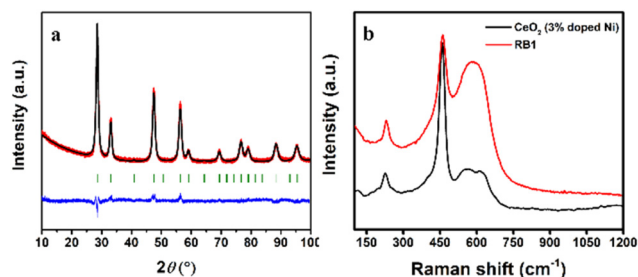

Fig. 12 Rietveld plot (a) and Raman spectroscopy (b) for 3% Ni-doped CeO_2.

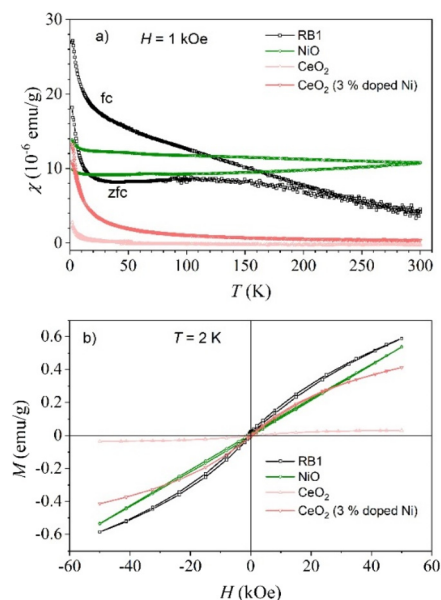

Fig. 13 Temperature dependent susceptibility (a) and isothermal magnetization (b) of CeO_2, NiO, RB1 and 3% Ni doped CeO_2.

final product (RB1) there is a lot of NiO and only a small portion of $Ce_{1-x}Ni_xO_2$, which makes the ferromagnet even more interesting as this small portion of $Ce_{1-x}Ni_xO_2$ makes a huge difference in the magnetic properties of the system.

Conclusions

The compound that corresponds to $CeNiO_3$ (RB1) was synthesized in a nanocrystalline form along with constituent oxides CeO_2 and NiO in order to resolve the structural issue regarding this compound. The recent literature claims that $CeNiO_3$ is a perovskite-type compound. However, XRD patterns from the $CeNiO_3$ perovskite suspiciously resemble the phase mixture of CeO_2 and NiO in a 1 : 1 molar ratio. Thus, we have tried to investigate this issue by proposing three different structural solutions. The first structural solution is that $CeNiO_3$ (RB1) is a two-phase system containing both cubic CeO_2 and NiO, the second one is that this two-phase system contains tetragonal solid solution $Ce_{1-x}Ni_xO_2$ and cubic NiO, while the final proposed solution is that $CeNiO_3$ (RB1) is actually a single-phase compound with a pyrochlore structure $Ce_2Ni_2O_7$, rather than a perovskite. According to the detailed structural and microstructural analysis, the most probable solution is that RB1 is a two-phase system comprising $Ce_{1-x}Ni_xO_2$ and NiO. The average crystallite size of RB1 is twice as small (around 5 nm) compared to the physical mixture of the constituent oxides (around 10 nm) in a molar ratio of 1 : 1. The involved elements in RB1 are homogeneously distributed along the surface. Raman spectroscopy reveals defects in RB1 that are probably related to symmetry breaking from the cubic to the tetragonal phase, which is the case when cubic CeO_2 is doped with Ni^{2+}. The magnetic properties also differ significantly: CeO_2 is diamagnetic, NiO is antiferromagnetic, and RB1 shows ferromagnetic behaviour.

Author contributions

J. K. conceptualization, formal analysis, and manuscript preparation; D. T. and S. Š. synthesis, thermogravimetric and X-ray diffraction measurements, and analysis; C. B. P. Raman spectra measurements and analysis; Z. J. magnetic property measurements and analysis; A. M. electron microscopy and diffraction; A. M. and I. A. extended X-ray absorption fine structure and X-ray absorption near edge structure measurements and analysis; M. M. and M. E. X-ray photoelectron spectroscopy measurements and analysis; A. A. powder XRD pattern analysis and structure solution; R. C. atomic pair distribution function measurements and analysis; I. Dj. Rietveld refinement, funding acquisition, project management; I. Dj., Á. K. and J. P. H. review, and editing.

Conflicts of interest

There are no conflicts to declare.

References

1 L. Wang, K. A. Stoerzinger, L. Chang, J. Zhao, Y. Li, C. S. Tang, X. Yin, M. E. Bowden, Z. Yang, H. Guo, L. You, R. Guo, J. Wang, K. Ibrahim, J. Chen, A. Rusydi, J. Wang, S. A. Chambers and Y. Du, Tuning Bifunctional Oxygen Electrocatalysts by Changing the A–Site Rare–Earth Element in Perovskite Nickelates, *Adv. Funct. Mater.*, 2018, **28**, 1803712.

2 D. K. Hwang, S. Kim, J.-H. Lee, I.-S. Hwang and I.-D. Kim, Phase evolution of perovskite $LaNiO_3$ nanofibers for supercapacitor application and p-type gas sensing properties of LaOCl–NiO composite nanofibers, *J. Mater. Chem.*, 2011, **21**, 1959–1965.

3 A. A. Yaremchenko, B. I. Arias-Serrano, K. Zakharchuk and J. R. Frade, Perovskite-like $LaNiO_{3-\delta}$ as Oxygen Electrode Material for Solid Oxide Electrolysis Cells, *ECS Trans.*, 2019, **91**, 2399–2408.

4 P. D. K. Nezhad, M. F. Bekheet, N. Bonmassar, A. Gili, F. Kamutzki, A. Gurlo, A. Doran, S. Schwarz, J. Bernardi, S. Praetz, A. Niaei, A. Farzi and S. Penner, Elucidating the role of earth alkaline doping in perovskite-based methane dry reforming catalysts, *Catal. Sci. Technol.*, 2022, **12**, 1229–1244.

5 F. J. Trindade, S. Damasceno, L. Otubo, M. R. Felez, D. Z. de Florio, F. C. Fonseca and A. S. Ferlauto, Tuning of Shape, Defects, and Disorder in Lanthanum-Doped Ceria Nanoparticles: Implications for High-Temperature Catalysis, *ACS Appl. Nano Mater.*, 2022, **5**, 8859–8867.

6 Z. Zhang, Y. Yu, X. Qiao, J. Sun, Y. Ni and J. Chen, Strongly correlated nickelate: Recent progress of synthesis and applications in artificial intelligence, *Mater. Sci. Semicond. Process.*, 2023, **166**, 107735.

7 G. Catalan, Progress in perovskite nickelate research, *Phase Transitions*, 2008, **81**, 729–749.

8 J. Chen, A. Bird, F. Yan, W. Wu, X. Ke, Y. Jiang and N. Chen, Mechanical and correlated electronic transport properties of preferentially orientated $SmNiO_3$ films, *Ceram. Int.*, 2020, **46**, 6693–6697.

9 D. D. Sarma, N. Shanthi and P. Mahadevan, Electronic structure and the metal-insulator transition in $LnNiO_3$ (Ln=La, Pr, Nd, Sm and Ho): bandstructure results, *J. Phys.: Condens.Matter*, 1994, **6**, 10467–10474.

10 A. Ambrosini and J.-F. Hamet, $Sm_xNd_{1−x}NiO_3$ thin-film solid solutions with tunable metal–insulator transition synthesized by alternate-target pulsed-laser deposition, *Appl. Phys. Lett.*, 2003, **82**, 727–729.

11 P. Laffez, M. Zaghrioui, I. Monot, T. Brousse and P. Lacorre, Microstructure and metal–insulator transition of $NdNiO_3$ thin films on various substrates, *Thin Solid Films*, 1999, **354**, 50–54.

12 F. Yan, Z. Mi, J. Chen, H. Hu, L. Gao, J. Wang, N. Chen, Y. Jiang, L. Qiao and J. Chen, Revealing the role of interfacial heterogeneous nucleation in the metastable thin film growth of rare-earth nickelate electronic transition materials, *Phys. Chem. Chem. Phys.*, 2022, **24**, 9333–9344.

13 X. Li, T. Zhang, Z. Li, F. Yan, H. Li, Y. Cui, N. Chen and J. Chen, Nonlinearity in regulating the metal to insulator transition of $ReNiO_3$ towards low temperature range, *Ceram. Int.*, 2022, **48**, 31995–32000.

14 Y. Bian, H. Li, F. Yan, H. Li, J. Wang, H. Zhang, Y. Jiang, N. Chen and J. Chen, Hydrogen induced electronic transition within correlated perovskite nickelates with heavy rare-earth composition, *Appl. Phys. Lett.*, 2022, **120**, 092103.

15 J. Chen, H. Hu, J. Wang, T. Yajima, B. Ge, X. Ke, H. Dong, Y. Jiang and N. Chen, Overcoming synthetic metastabilities and revealing metal-to-insulator transition & thermistor bi-functionalities for d-band correlation perovskite nickelates, *Mater. Horiz.*, 2019, **6**, 788–795.

16 N. Shukla, T. Joshi, S. Dasgupta, P. Borisov, D. Lederman and S. Datta, Electrically induced insulator to metal transition in epitaxial $SmNiO_3$ thin films, *Appl. Phys. Lett.*, 2014, **105**, 012108.

17 F. Y. Bruno, S. Valencia, R. Abrudan, Y. Dumont, C. Carrétéro, M. Bibes and A. Barthélémy, Probing the metal-insulator transition in nickelates using soft x-ray absorption spectroscopy, *Appl. Phys. Lett.*, 2014, **104**, 021920.

18 M. T. Escote, A. M. L. da Silva, J. R. Matos and R. F. Jardim, General Properties of Polycrystalline $LnNiO_3$ (Ln=Pr, Nd, Sm) Compounds Prepared through Different Precursors, *J. Solid State Chem.*, 2000, **151**, 298–307.

19 T. Moriga, O. Usaka, I. Nakabayashi, Y. Hirashima, T. Kohno, S. Kikkawa and F. Kanamaru, Reduction of the perovskite-type $LnNiO_3$ (Ln=Pr, Nd) to $Ln_3Ni_3O_7$ with monovalent nickel ions, *Solid State Ionics*, 1994, **74**, 211–217.

20 M. P. Harikrishnan and A. C. Bose, Porous $CeNiO_3$ with an enhanced electrochemical performance and prolonged cycle life (>50 000 cycles) via a lemon-assisted sol–gel autocombustion method, *New J. Chem.*, 2022, **46**, 15118–15129.

21 M. P. Harikrishnan, A. J. C. Mary and A. C. Bose, Electrochemical performance of $ANiO_3$ (A= La, Ce) perovskite oxide material and its device performance for supercapattery application, *Electrochim. Acta*, 2020, **362**, 137095.

22 N. Ahmad, F. Alharthi, M. Alam, R. Wahab, S. Manoharadas and B. Alrayes, Syngas Production via CO_2 Reforming of Methane over $SrNiO_3$ and $CeNiO_3$ Perovskites, *Energies*, 2021, **14**, 2928.

23 H.-N. Barad, D. A. Keller, K. J. Rietwyk, A. Ginsburg, S. Tirosh, S. Meir, A. Y. Anderson and A. Zaban, How Transparent Oxides Gain Some Color: Discovery of a $CeNiO_3$ Reduced Bandgap Phase as an Absorber for Photovoltaics, *ACS Comb. Sci.*, 2018, **20**, 366–376.

24 N. Ahmad, R. Wahab, S. Manoharadas, B. F. Alrayes, M. Alam and F. A. Alharthi, The Role of Strontium in $CeNiO_3$ Nano-Crystalline Perovskites for Greenhouse Gas Mitigation to Produce Syngas, *Molecules*, 2022, **27**, 356.

25 N. Tri, N. P. Anh, T. D. Huy, D. B. Long, H. C. Anh, P. H. Phuong, N. T. T. Van, T.-T. Nguyen and L. C. Loc, In situ synthesis of highly effective nickel nanocatalyst for methane bireforming, *J. Sci.: Adv. Mater. Devices*, 2023, **8**, 100529.

26 M. P. Harikrishnan and A. C. Bose, Co-precipitation route for synthesizing $CeNiO_3$ and its application as excellent pseudocapacitor, *AIP Conf. Proc.*, 2020, **2265**, 030631.

27 M. P. Harikrishnan and A. C. Bose, Binder–free synthesis of cerium nickel oxide for supercapattery devices, *Int. J. Energy Res.*, 2022, **46**, 21826–21840.

28 T. C. Huang, W. Parrish, H. Toraya, P. Lacorre and J. B. Torrance, High-temperature crystal structures of orthorhombic and rhombohedral $PrNiO_3$, *Mater. Res. Bull.*, 1990, **25**, 1091–1098.

29 V. Vibhu, A. Flura, C. Nicollet, S. Fourcade, N. Penin, J.-M. Bassat, J.-C. Grenier, A. Rougier and M. Pouchard, Characterization of $PrNiO_{3−δ}$ as oxygen electrode for SOFCs, *Solid State Sci.*, 2018, **81**, 26–31.

30 J. A. Alonso, M. J. Martínez-Lope, M. T. Casais, M. A. G. Aranda and M. T. Fernández-Díaz, Metal–Insulator Transitions, Structural and Microstructural Evolution of $RNiO_3$ (R = Sm, Eu, Gd, Dy, Ho, Y) Perovskites: Evidence for Room-Temperature Charge Disproportionation in Monoclinic $HoNiO_3$ and $YNiO_3$, *J. Am. Chem. Soc.*, 1999, **121**, 4754–4762.

31 S. J. Kashyap, R. Sankannavar and G. M. Madhu, Synthesis and Characterization of La(Ce, Ba)NiO_3 Perovskite-Type Oxides, *J. Supercond. Novel Magn.*, 2022, **35**, 2107–2118.

32 Sk. Mahammadunnisa, P. M. K. Reddy, N. Lingaiah and Ch. Subrahmanyam, $NiO/Ce_{1−x}Ni_xO_{2−δ}$ as an alternative to noble metal catalysts for CO oxidation, *Catal. Sci. Technol.*, 2013, **3**, 730–736.

33 L. Barrio, A. Kubacka, G. Zhou, M. Estrella, A. Martínez-Arias, J. C. Hanson, M. Fernández-García and

J. A. Rodriguez, Unusual Physical and Chemical Properties of Ni in $Ce_{1-x}Ni_xO_{2-y}$ Oxides: Structural Characterization and Catalytic Activity for the Water Gas Shift Reaction, *J. Phys. Chem. C*, 2010, **114**, 12689–12697.

34 G. Zhou, L. Barrio, S. Agnoli, S. D. Senanayake, J. Evans, A. Kubacka, M. Estrella, J. C. Hanson, A. Martínez-Arias, M. Fernández-García and J. A. Rodriguez, High Activity of $Ce_{1-x}Ni_xO_{2-y}$ for H_2 Production through Ethanol Steam Reforming: Tuning Catalytic Performance through Metal-Oxide Interactions, *Angew. Chem., Int. Ed.*, 2010, **49**, 9680–9684.

35 J. Milikić, R. O. Fuentes, J. E. Tasca, D. M. F. Santos, B. Šljukić and F. M. L. Figueiredo, Nickel-Doped Ceria Bifunctional Electrocatalysts for Oxygen Reduction and Evolution in Alkaline Media, *Batteries*, 2022, **8**, 100.

36 W. Shan, M. Fleys, F. Lapicque, D. Swierczynski, A. Kiennemann, Y. Simon and P.-M. Marquaire, Syngas production from partial oxidation of methane over $Ce_{1-x}Ni_xO_Y$ catalysts prepared by complexation–combustion method, *Appl. Catal., A*, 2006, **311**, 24–33.

37 L. Pino, A. Vita, F. Cipitì, M. Laganà and V. Recupero, Catalytic Performance of $Ce_{1-x}Ni_xO_2$ Catalysts for Propane Oxidative Steam Reforming, *Catal. Lett.*, 2008, **122**, 121–130.

38 Z. V. Popović, Z. D. Dohčević-Mitrović, N. Paunović and M. Radović, Evidence of charge delocalization in $Ce_{1-x}Fe_x^{2+(3+)}O_{2-y}$ nanocrystals (x = 0, 0.06, 0.12), *Phys. Rev. B: Condens. Matter Mater. Phys.*, 2012, **85**, 014302.

39 S. K. Misra, S. I. Andronenko, M. H. Engelhard, A. Thurber, K. M. Reddy and A. Punnoose, Role of dopant incorporation on the magnetic properties of $Ce_{1-x}Ni_xO_2$ nanoparticles: An electron paramagnetic resonance study, *J. Appl. Phys.*, 2008, **103**(7), 07D122.

40 Y. Wang, A. Zhu, Y. Zhang, C. T. Au, X. Yang and C. Shi, Catalytic reduction of NO by CO over NiO/CeO_2 catalyst in stoichiometric NO/CO and $NO/CO/O_2$ reaction, *Appl. Catal., B*, 2008, **81**, 141–149.

41 R. Rameshan, P. Pentyala, S. A. Singh, P. A. Deshpande and S. Roy, Probing the surface active sites of $Ce_{1-x}Ni_xO_{2-\delta}$ for catalytic reduction of NO, *J. Environ. Chem. Eng.*, 2022, **10**, 108966.

42 J. Kojčinović, M. Sahu, S. Hajra, D. Tatar, T. Klaser, Ž. Skoko, Z. Jagličić, E. Sadrollahi, F. J. Litterst, H. J. Kim and I. Djerdj, Nanocrystalline triple perovskite compounds $A_3Fe_2BO_9$ (A = Sr, Ba; B = W, Te) with ferromagnetic and dielectric properties for triboelectric energy harvesting, *Mater. Chem. Front.*, 2022, **6**, 1116–1128.

43 D. Tatar, J. Kojčinović, B. Marković, A. Széchenyi, A. Miletić, S. B. Nagy, S. Ziegenheim, I. Szenti, A. Sapi, Á. Kukovecz, K. Dinjar, Y. Tang, D. Stenzel, G. Varga and I. Djerdj, Sol-Gel Synthesis of Ceria-Zirconia-Based High-Entropy Oxides as High-Promotion Catalysts for the Synthesis of 1,2-Diketones from Aldehyde, *Molecules*, 2021, **26**, 6115.

44 J. Bijelić, A. Stanković, M. Medvidović-Kosanović, B. Marković, P. Cop, Y. Sun, S. Hajra, M. Sahu,

45 J. Vukmirović, D. Marković, Á. Kukovecz, Z. Jagličić, B. M. Smarsly and I. Djerdj, Rational Sol–Gel-Based Synthesis Design and Magnetic, Dielectric, and Optical Properties Study of Nanocrystalline $Sr_3Co_2WO_9$ Triple Perovskite, *J. Phys. Chem. C*, 2020, **124**, 12794–12807.

45 J. Bijelić, D. Tatar, S. Hajra, M. Sahu, S. J. Kim, Z. Jagličić and I. Djerdj, Nanocrystalline Antiferromagnetic High-κ Dielectric Sr_2NiMO_6 (M = Te, W) with Double Perovskite Structure Type, *Molecules*, 2020, **25**, 3996.

46 J. Bijelić, A. Stanković, B. Matasović, B. Marković, M. Bijelić, Ž. Skoko, J. Popović, G. Štefanić, Z. Jagličić, S. Zellmer, T. Preller, G. Garnweitner, T. Đorđević, P. Cop, B. Smarsly and I. Djerdj, Structural characterization and magnetic property determination of nanocrystalline $Ba_3Fe_2WO_9$ and $Sr_3Fe_2WO_9$ perovskites prepared by a modified aqueous sol–gel route, *CrystEngComm*, 2019, **21**, 218–227.

47 J. Bijelić, D. Tatar, M. Sahu, Z. Jagličić and I. Djerdj, Size reduction-induced properties modifications of antiferromagnetic dielectric nanocrystalline Ba_2NiMO_6 (M = W, Te) double perovskites, *Oxford Open Mater. Sci.*, 2021, **1**(1), itaa003.

48 S. Nundy, D. Tatar, J. Kojčinović, H. Ullah, A. Ghosh, T. K. Mallick, R. Meinusch, B. M. Smarsly, A. A. Tahir and I. Djerdj, Bandgap Engineering in Novel Fluorite–Type Rare Earth High–Entropy Oxides (RE–HEOs) with Computational and Experimental Validation for Photocatalytic Water Splitting Applications, *Adv. Sustainable Syst.*, 2022, **6**, 2200067.

49 N. Fairley, V. Fernandez, M. Richard-Plouet, C. Guillot-Deudon, J. Walton, E. Smith, D. Flahaut, M. Greiner, M. Biesinger, S. Tougaard, D. Morgan and J. Baltrusaitis, Systematic and collaborative approach to problem solving using X-ray photoelectron spectroscopy, *Appl. Surf. Sci. Adv.*, 2021, **5**, 100112.

50 B. Ravel and M. Newville, *ATHENA*, ARTEMIS, HEPHAESTUS : data analysis for X-ray absorption spectroscopy using IFEFFIT, *J. Synchrotron Radiat.*, 2005, **12**, 537–541.

51 J. J. Rehr, R. C. Albers and S. I. Zabinsky, High-order multiple-scattering calculations of x-ray-absorption fine structure, *Phys. Rev. Lett.*, 1992, **69**, 3397–3400.

52 C. Prescher and V. B. Prakapenka, DIOPTAS : a program for reduction of two-dimensional X-ray diffraction data and data exploration, *High Pressure Res.*, 2015, **35**, 223–230.

53 P. Juhás, T. Davis, C. L. Farrow and S. J. L. Billinge, *PDFgetX3*: a rapid and highly automatable program for processing powder diffraction data into total scattering pair distribution functions, *J. Appl. Crystallogr.*, 2013, **46**, 560–566.

54 C. L. Farrow, P. Juhas, J. W. Liu, D. Bryndin, E. S. Božin, J. Bloch, T. Proffen and S. J. L. Billinge, PDFfit2 and PDFgui: computer programs for studying nanostructure in crystals, *J. Phys.: Condens.Matter*, 2007, **19**, 335219.

55 P. E. Raison, C. C. Pavel, R. Jardin, E. Suard, R. G. Haire and K. Popa, Thermal expansion behavior of $Ce_2Zr_2O_7$ up to

898 K in conjunction with structural analyses by neutron diffraction, *Phys. Chem. Miner.*, 2010, **37**, 555–559.

56 Database of Ionic Radii, https://abulafia.mt.ic.ac.uk/shannon/ptable.php.

57 H. Zhou, P. Hu, Z. Huang, F. Qin, W. Shen and H. Xu, Preparation of NiCe Mixed Oxides for Catalytic Decomposition of N_2O, *Ind. Eng. Chem. Res.*, 2013, **52**, 4504–4509.

58 R. K. Pati, I. C. Lee, S. Hou, O. Akhuemonkhan, K. J. Gaskell, Q. Wang, A. I. Frenkel, D. Chu, L. G. Salamanca-Riba and S. H. Ehrman, Flame Synthesis of Nanosized Cu−Ce−O, Ni−Ce−O, and Fe−Ce−O Catalysts for the Water-Gas Shift (WGS) Reaction, *ACS Appl. Mater. Interfaces*, 2009, **1**, 2624–2635.

59 P. Cop, R. Maile, Y. Sun, O. Khalid, I. Djerdj, P. Esch, S. Heiles, H. Over and B. M. Smarsly, Impact of Aliovalent/Isovalent Ions (Gd, Zr, Pr, and Tb) on the Catalytic Stability of Mesoporous Ceria in the HCl Oxidation Reaction, *ACS Appl. Nano Mater.*, 2020, **3**, 7406–7419.

60 M. Varenik, J. C. Nino, E. Wachtel, S. Kim, O. Yeheskel, N. Yavo and I. Lubomirsky, Dopant Concentration Controls Quasi-Static Electrostrictive Strain Response of Ceria Ceramics, *ACS Appl. Mater. Interfaces*, 2020, **12**, 39381–39387.

61 R. Schmitt, A. Nenning, O. Kraynis, R. Korobko, A. I. Frenkel, I. Lubomirsky, S. M. Haile and J. L. M. Rupp, A review of defect structure and chemistry in ceria and its solid solutions, *Chem. Soc. Rev.*, 2020, **49**, 554–592.

62 E. Kroumova, M. I. Aroyo, J. M. Perez-Mato, A. Kirov, C. Capillas, S. Ivantchev and H. Wondratschek, Bilbao Crystallographic Server: Useful Databases and Tools for Phase-Transition Studies, *Phase Transitions*, 2003, **76**, 155–170.

63 Q. Zhou, C. Zhou, Y. Zhou, W. Hong, S. Zou, X. Q. Gong, J. Liu, L. Xiao and J. Fan, More than oxygen vacancies: A collective crystal-plane effect of CeO_2 in gas-phase selective oxidation of benzyl alcohol, *Catal. Sci. Technol.*, 2019, **9**, 2960–2967.

64 K. Kuntaiah, P. Sudarsanam, B. M. Reddy and A. Vinu, Nanocrystalline $Ce_{1-x}Sm_xO_{2-\delta}$ (x = 0.4) solid solutions: Structural characterization versus CO oxidation, *RSC Adv.*, 2013, **3**, 7953–7962.

65 O. V. Safonova, A. Guda, Y. Rusalev, R. Kopelent, G. Smolentsev, W. Y. Teoh, J. A. van Bokhoven and M. Nachtegaal, Elucidating the Oxygen Activation Mechanism on Ceria-Supported Copper-Oxo Species Using Time-Resolved X-ray Absorption Spectroscopy, *ACS Catal.*, 2020, **10**, 4692–4701.

66 N. Shehata, K. Meehan, M. Hudait and N. Jain, Control of oxygen vacancies and Ce^{+3} concentrations in doped ceria nanoparticles via the selection of lanthanide element, *J. Nanopart. Res.*, 2012, **14**, 1173.

67 S. Tiwari, G. Rathore, N. Patra, A. K. Yadav, D. Bhattacharya, S. N. Jha, C. M. Tseng, S. W. Liu, S. Biring and S. Sen, Oxygen and cerium defects mediated changes in structural, optical and photoluminescence pro-

perties of Ni substituted CeO_2, *J. Alloys Compd.*, 2019, **782**, 689–698.

68 X. Wang, J. C. Hanson, G. Liu, J. A. Rodriguez, A. Iglesias-Juez and M. Fernández-García, The behavior of mixed-metal oxides: Physical and chemical properties of bulk $Ce_{1-x}Tb_xO_2$ and nanoparticles of $Ce_{1-x}Tb_xO_y$, *J. Chem. Phys.*, 2004, **121**, 5434–5444.

69 M. Yashima, H. Arashi, M. Kakihana and M. Yoshimura, Raman Scattering Study of Cubic-Tetragonal Phase Transition in $Zr_{1-x}Ce_xO_2$ Solid Solution, *J. Am. Chem. Soc.*, 1994, **77**, 1067–1071.

70 L. Atzori, M. G. Cutrufello, D. Meloni, C. Cannas, D. Gazzoli, R. Monaci, M. F. Sini and E. Rombi, Highly active $NiO-CeO_2$ catalysts for synthetic natural gas production by CO_2 methanation, *Catal. Today*, 2018, **299**, 183–192.

71 J. Deng, W. Chu, B. Wang, W. Yang and X. S. Zhao, Mesoporous $Ni/Ce_{1-x}Ni_xO_{2-y}$ heterostructure as an efficient catalyst for converting greenhouse gas to H_2 and syngas, *Catal. Sci. Technol.*, 2016, **6**, 851–862.

72 W. Shan, Reduction property and catalytic activity of $Ce_{1-x}Ni_xO_2$ mixed oxide catalysts for CH_4 oxidation, *Appl. Catal., A*, 2003, **246**, 1–9.

73 C. Schilling, A. Hofmann, C. Hess and M. V. Ganduglia-Pirovano, Raman Spectra of Polycrystalline CeO_2 : A Density Functional Theory Study, *J. Phys. Chem. C*, 2017, **121**, 20834–20849.

74 G. George and S. Anandhan, Synthesis and characterisation of nickel oxide nanofibre webs with alcohol sensing characteristics, *RSC Adv.*, 2014, **4**, 62009–62020.

75 H.-T. Vu, I. Arčon, D. O. de Souza, S. Pollastri, G. Dražić, J. Volavšek, G. Mali, N. Z. Logar and N. N. Tušar, Insight into the interdependence of Ni and Al in bifunctional Ni/ZSM-5 catalysts at the nanoscale, *Nanoscale Adv.*, 2022, **4**, 2321–2331.

76 S. Sasaki, K. Fujino and Y. Takéuchi, X-ray determination of electron-density distributions in oxides, MgO, MnO, CoO, and NiO, and atomic scattering factors of their constituent atoms, *Proc. Jpn. Acad., Ser. B*, 1979, **55**, 43–48.

77 M. Zabilskiy, I. Arčon, P. Djinović, E. Tchernychova and A. Pintar, *In-situ* XAS Study of Catalytic N_2O Decomposition Over CuO/CeO_2 Catalysts, *ChemCatChem*, 2021, **13**, 1814–1823.

78 T. Nakano, A. Kotani and J. C. Parlebas, Theory of XPS and BIS Spectra in Ce_2O_3 and CeO_2, *J. Phys. Soc. Jpn.*, 1987, **56**, 2201–2210.

79 F. de Groot, Multiplet effects in X-ray spectroscopy, *Coord. Chem. Rev.*, 2005, **249**, 31–63.

80 M. A. van Veenendaal and G. A. Sawatzky, Nonlocal screening effects in 2*p* x-ray photoemission spectroscopy core-level line shapes of transition metal compounds, *Phys. Rev. Lett.*, 1993, **70**, 2459–2462.

81 D. R. Mullins, The surface chemistry of cerium oxide, *Surf. Sci. Rep.*, 2015, **70**, 42–85.

82 P. Dubey, N. Kaurav, R. S. Devan, G. S. Okram and Y. K. Kuo, The effect of stoichiometry on the structural,

thermal and electronic properties of thermally decomposed nickel oxide, *RSC Adv.*, 2018, **8**, 5882–5890.

83 U. De Silva, J. See, W. P. R. Liyanage, J. Masud, J. Wu, W. Yang, W.-T. Chen, D. Prendergast and M. Nath, Understanding the Structural Evolution of a Nickel Chalcogenide Electrocatalyst Surface for Water Oxidation, *Energy Fuels*, 2021, **35**, 4387–4403.

84 P. S. Bagus, C. J. Nelin, C. R. Brundle, B. V. Crist, E. S. Ilton, N. Lahiri and K. M. Rosso, Main and Satellite Features in the Ni 2p XPS of NiO, *Inorg. Chem.*, 2022, **61**, 18077–18094.

85 X. Xu, L. Li, J. Huang, H. Jin, X. Fang, W. Liu, N. Zhang, H. Wang and X. Wang, Engineering Ni^{3+} Cations in NiO Lattice at the Atomic Level by Li + Doping: The Roles of Ni^{3+} and Oxygen Species for CO Oxidation, *ACS Catal.*, 2018, **8**, 8033–8045.

86 B. Savova, S. Loridant, D. Filkova and J. M. M. Millet, Ni–Nb–O catalysts for ethane oxidative dehydrogenation, *Appl. Catal., A*, 2010, **390**, 148–157.

87 V. Pfeifer, T. E. Jones, S. Wrabetz, C. Massué, J. J. V. Vélez, R. Arrigo, M. Scherzer, S. Piccinin, M. Hävecker, A. Knop-Gericke and R. Schlögl, Reactive oxygen species in iridium-based OER catalysts, *Chem. Sci.*, 2016, **7**, 6791–6795.

88 V. Pfeifer, T. E. Jones, J. J. V. Vélez, R. Arrigo, S. Piccinin, M. Hävecker, A. Knop-Gericke and R. Schlögl, In situ observation of reactive oxygen species forming on oxygen-evolving iridium surfaces, *Chem. Sci.*, 2017, **8**, 2143–2149.

89 J. Rossmeisl, Z.-W. Qu, H. Zhu, G.-J. Kroes and J. K. Nørskov, Electrolysis of water on oxide surfaces, *J. Electroanal. Chem.*, 2007, **607**, 83–89.

90 S. Piccinin, A. Sartorel, G. Aquilanti, A. Goldoni, M. Bonchio and S. Fabris, Water oxidation surface mechanisms replicated by a totally inorganic tetraruthenium–oxo molecular complex, *Proc. Natl. Acad. Sci. U. S. A.*, 2013, **110**, 4917–4922.

91 E. Ioannidou, Ch. Neofytidis, L. Sygellou and D. K. Niakolas, Au-doped Ni/GDC as an Improved Cathode Electrocatalyst for H_2O Electrolysis in SOECs, *Appl. Catal., B*, 2018, **236**, 253–264.

92 G. J. Kim, S. M. Lee, S. C. Hong and S. S. Kim, Active oxygen species adsorbed on the catalyst surface and its effect on formaldehyde oxidation over Pt/TiO_2 catalysts at

room temperature; role of the Pt valence state on this reaction?, *RSC Adv.*, 2018, **8**, 3626–3636.

93 K. Ackland and J. M. D. Coey, Room temperature magnetism in CeO_2 —A review, *Phys. Rep.*, 2018, **746**, 1–39.

94 L. R. Shah, B. Ali, H. Zhu, W. G. Wang, Y. Q. Song, H. W. Zhang, S. I. Shah and J. Q. Xiao, Detailed study on the role of oxygen vacancies in structural, magnetic and transport behavior of magnetic insulator: Co–CeO_2, *J. Phys.: Condens. Matter*, 2009, **21**, 486004.

95 A. Barbier, C. Mocuta, W. Neubeck, M. Mulazzi, F. Yakhou, K. Chesnel, A. Sollier, C. Vettier and F. de Bergevin, Surface and Bulk Spin Ordering of Antiferromagnetic Materials: NiO(111), *Phys. Rev. Lett.*, 2004, **93**, 257208.

96 M. Jagodič, Z. Jagličić, A. Jelen, J. B. Lee, Y.-M. Kim, H. J. Kim and J. Dolinšek, Surface-spin magnetism of antiferromagnetic NiO in nanoparticle and bulk morphology, *J. Phys.: Condens. Matter*, 2009, **21**, 215302.

97 P. L. Madhav, K. R. Teja, N. Sreelekha, D. A. Reddy, G. Murali, M. Ramanadha, K. Subramanyam and R. P. Vijayalakshmi, Transition of Magnetic Characteristics from Paramagnetic State to Ferromagnetic Phase in $Ce_{1-x}Ni_xO_2$ Nanoparticles, *J. Supercond. Novel Magn.*, 2018, **31**, 1631–1636.

98 M. Parveen, V. Asvini, G. Saravanan, K. Ravichandran and D. KalaiSelvi, Investigation of Ni-doped CeO_2 nanoparticles–spintronics application, *Ionics*, 2017, **23**, 1285–1291.

99 A. Thurber, K. M. Reddy, V. Shutthanandan, M. H. Engelhard, C. Wang, J. Hays and A. Punnoose, Ferromagnetism in chemically synthesized CeO_2 nanoparticles by Ni doping, *Phys. Rev. B: Condens. Matter Mater. Phys.*, 2007, **76**, 165206.

100 R. Murugan, G. Vijayaprasath, T. Mahalingam and G. Ravi, Room temperature ferromagnetism of Ni doped cerium oxide single crystalline thin Films deposited by using rf magnetron sputtering, *Mater. Lett.*, 2016, **162**, 71–74.

101 F. Abbas, T. Jan, J. Iqbal, I. Ahmad, M. S. H. Naqvi and M. Malik, Facile synthesis of ferromagnetic Ni doped CeO_2 nanoparticles with enhanced anticancer activity, *Appl. Surf. Sci.*, 2015, **357**, 931–936.